

**Lidar observations of the middle atmospheric thermal tides and
comparison with HRDI and GSWM.**

**Part I: Methodology and winter observations at Table Mountain
(34.4°N).**

Thierry Leblanc ¹, I. Stuart McDermid ¹, and David A. Ortland ²

¹ Jet Propulsion Laboratory
California Institute of Technology
Table Mountain Facility
Wrightwood, CA 92397

² Space Physics Research Laboratory
Department of Atmospheric, Oceanic and Space Sciences
University of Michigan
Ann Arbor, MI 48109-2143

To be Submitted to the Journal of Geophysical Research-Atmospheres, June 1998

Abstract

The tidal signature in the middle atmospheric thermal structure is investigated using more than 140 hours of nighttime lidar measurements at Table Mountain (34.4°N) during January 1997 and February 1998. The lidar profiles (30-85 km) reveal the presence of persistent mesospheric temperature inversions around 65-70 km altitude with a clear Local-Solar-Time (LST) dependence. Daytime temperature profiles (65-105 km) obtained by the High Resolution Doppler Imager (HRDI) onboard the Upper Atmosphere Research Satellite (UARS) in January and February from 1994 to 1997 and zonally averaged at the latitude of TMF are considered together with the lidar results. The daytime HRDI and nighttime lidar temperature differences from their respective daytime and nighttime averages are compared to the equivalent differences predicted by the Global Scale Wave Model (GSWM). A remarkable consistency is observed between the lidar and the HRDI upper mesospheric thermal structure, with a continuous downward propagation of warm temperatures from 100 km at 10:00 LST to 75 km at 20:00 LST and 65-70 km at 3:00-5:00 LST surrounded above and below by colder temperatures. This structure is predicted by GSWM but with a 2-4 hour delay and a weaker amplitude. On the lower side of this structure (i.e. 65-70 km) a thin layer, characterized by early night cold temperatures and late night warm temperatures, is identified as the result of the downward propagation of the temperature inversions. Using simulated data and a "first-guess" method, and assuming that the observed temperature variability was entirely driven by tides, some estimations of the diurnal and semidiurnal phases and amplitudes have been made from the lidar measurements between 40 and 85 km altitude. The estimated diurnal amplitude exhibits a minimum at 63 km with a fast phase transition characteristic of the transition between the upper stratospheric trapped modes (phase at 18:00 LST) and the upward propagating modes. This transition layer is predicted by GSWM to be at 5 km lower altitude, altitude shift present throughout the middle mesosphere. Immediately above the transition layer the very fast growing diurnal amplitude between 65 and 72 km is followed by a substantial decrease and by the emergence of the semidiurnal component resulting in the formation of the mesospheric temperature inversion layers. However, the amplitude of the inversions

remains large compared to the theoretical tidal predictions and a different formation mechanism should possibly be considered. Recent modeling studies show that gravity wave breaking can be significantly affected by the tidal background winds and some preferential wave breaking times could emerge that are dependent on the phase of the diurnal tide and the characteristics of the dissipating waves. This "LST-filtering" could result in LST-dependent temperature inversion layers similar to those observed by lidar.

1. Introduction

Atmospheric tides are the global, latitudinally-dependent response of the atmosphere to the periodic forcing of solar heating. They comprise Fourier-decomposed oscillations with periods that are harmonics of the initial 24-hour period forcing, i.e., 24-hours, 12-hours, 8-hours, etc.. Tide theories, and many associated mechanistic models, have been extensively developed [e.g., *Chapman and Lindzen*, 1970; *Forbes*, 1982; *Hagan et al.*, 1995] and predict the dominance of the 24-h (diurnal) and 12-h (semidiurnal) westward migrating modes (following the apparent motion of the sun). An interesting overview of tidal theory is given by *Forbes* [1995]. Ideally the tides should be studied using continuous and simultaneous global measurements with a latitudinal resolution of a few degrees. Unfortunately, no such ideal instrument or network of instruments is presently available and probably will not exist for some time. Satellite measurements have the advantage of providing global coverage but their time-sampling is usually inadequate and the data needs to be averaged over several days or months to complete a full 24-hour cycle. On the other hand, the localized ground-based measurements can be obtained continuously over a longer period (many days in a row) but their interpretation in terms of tides is subject to bias due to regional effects such as inertio-gravity waves and gravity waves with long periods (8- to 48-hours) and the inability to retrieve global information. Although the sources of the middle atmospheric tides (10-100 km) are located in the troposphere (near-IR absorption by water vapor) and stratosphere (UV absorption by ozone), their amplitudes are much larger once they have propagated upward into the Mesosphere-Lower-Thermosphere (MLT) region. Consequently, tidal oscillations in the MLT region have been widely observed in the horizontal wind data [e.g., *Manson et al.*, 1989; *Burrage et al.*, 1995; *McLandress et al.*, 1996; *Khattatov et al.*, 1997] but very few observations of the middle atmospheric and MLT thermal tides have been obtained until recently [*Gille et al.*, 1991; *Dudhia et al.*, 1993; *Keckhut et al.*, 1996; *Yu et al.*, 1997; *States and Gardner*, 1998; *Meriwether et al.*, 1998]. The number of instruments and reliable temperature measurements techniques for these altitudes is limited, especially at latitudes lower than 40°N. There is a crucial need for extensive studies of the thermal tides in the stratosphere and mesosphere

in order to quantify their importance and their role in the middle atmospheric dynamics as well as to better understand the MLT coupling (the MLT region has not yet lost its nickname of "ignorosphere").

In this study, nighttime winter temperature profiles (30-95 km) obtained by the Jet Propulsion Laboratory (JPL) Rayleigh lidar located at the Table Mountain Facility, California (TMF, 34.4°N) [McDermid *et al.*, 1990], and daytime temperature profiles (60-110 km) from the High Resolution Doppler Interferometer (HRDI) [Ortland *et al.*, 1998] onboard the Upper Atmosphere Research Satellite (UARS) have been compared to the January outputs of the Global Scale Wave Model (GSWM) [Hagan *et al.*, 1995]. The study focuses on the lidar results since the HRDI data set remains statistically limited. Although measurements of the middle atmospheric temperature by lidar are very accurate up to ~80 km altitude, the extraction of thermal tidal components is usually difficult and painstaking for several reasons:

- i) The amplitude of the middle atmospheric tides is believed to be less than 5-10 K and many other real geophysical features (mostly long-period gravity waves) can be important sources of "geophysical noise" obscuring the tidal signatures. These interfering features are readily seen because of the high accuracy, and vertical and temporal resolutions of the lidar measurements.
- ii) The tidal amplitudes usually increase with altitude but so does the total error in the lidar retrieval of temperature.
- iii) For most lidar systems only nighttime measurements are available making the extraction of the 12-hour and 24-hour components more difficult.

The problem (iii) similarly applies to the daytime-only HRDI temperature measurements.

Unless a strong tidal component is obvious from the observations, simply studying the time-evolution of the temperature during single nights or single days is not a good way to investigate tides and a more sophisticated approach has to be taken. To reduce the effect of problems (i) and (ii), the first step involves taking several nights (days) of lidar (HRDI) measurements during a given season and summing the raw

data taken at given Local Solar Times (LST) to obtain mean temperature profiles as a function of LST. Thus, most of the long-period gravity wave disturbances detected by lidar, most of the variability due to the planetary waves detected by HRDI, and most of the lidar and HRDI instrumental noise, which are expected to be random from one night (day) to another, are substantially reduced if not removed. To reduce the effect of problem (iii) several approaches have been used in this study. The classical method would be to take a known climatology like CIRA86 [Fleming *et al.*, 1990] or MSIS90 [Hedin, 1991] as the 24-hour average and reference profile. However, several lidar temperature climatologies have shown large disagreements between CIRA86 and the observations [Leblanc *et al.*, 1998b] so that the reference profile would actually be wrong. The same argument applies to MSIS90 since it includes some CIRA86 information in its middle atmospheric part. For this reason we choose not to use any a priori information but only information based on the observations. First, using the mean profiles, the HRDI temperature differences from the daytime average (~8 hours) and the lidar temperature differences from the nighttime average (10-11 hours) were calculated as a function of LST and then were combined and compared. Second, these differences were compared to corresponding values calculated from outputs of GSWM. Third, the lidar temperature differences were fitted iteratively, using estimations of the tidal phases and amplitudes, to extract both diurnal and semidiurnal components. No such work was attempted for the HRDI differences since the measurement window was only 8 hours. Some computer simulations of tide extraction were performed beforehand to insure that the iterative extraction of the 12- and 24-hour components was possible even when using only a 10-11 hour long nighttime measurement window. The same method has been used for a similar study using lidar data from Mauna Loa Observatory (19.5°N) in October and is presented in a companion paper [Leblanc *et al.*, this issue ?].

2. Instruments and Data sets

2.1. Rayleigh lidar temperatures

Laser radiation transmitted into the atmosphere is backscattered by the molecules in the atmosphere and collected by a telescope. When the Mie scattering due to the aerosols particles is negligible compared to the molecular scattering (i.e. above 30 km) the number of photons received is proportional to the number of photons emitted in the laser pulse and to the number of air molecules (or air density). The atmospheric relative density can thus be derived (Rayleigh lidar equation). The temperature is deduced from the relative density using the hydrostatic equilibrium and ideal gas law assumptions. A priori temperature information is needed at the top of the profile and is usually taken from climatological models like CIRA-86. The total error in the temperature at the top due to this a priori initialization can be larger than 20 K but rapidly decreases as the temperature profile is integrated downward (typically divided by a factor of 3 every 10 km). Some description of the Rayleigh lidar, temperature retrieval techniques, and detailed reviews of the different sources of temperature uncertainty are given, for example, by *Leblanc et al.* [1998a] and *Keckhut et al.* [1990]. The JPL Rayleigh lidar instrument used in this study is located at Table Mountain Facility, California (TMF, 34.4°N, 117.7°W). In this study we focus on the winter period. Lidar temperature profiles obtained during 5 nights from January 7-11, 1997, and 7 nights between February 26 and March 4, 1998 were used, with a maximum of 11-hours of continuous measurements per night. A total of 140 hours of lidar measurements distributed from 18:00 to 5:00 LST were available.

2.2. HRDI temperatures

HRDI measures brightnesses in the O₂ atmospheric A-band by observing the earth limb with line of sight tangent heights between 50 and 115 km. This brightness is basically proportional to both the band volume emission rate and an emission cross section which is a function of temperature and the emission line within the band. In order to separate the brightness dependence on volume emission rate and temperature,

two consecutive limb scans are made in which different lines within the A-band are measured. The profiles of brightness measurements from the two limb scans are inverted together to provide both a temperature and a band volume emission rate profile. Because of the nature of the viewing modes, temperatures are recovered from 65 to 105 km, with the most accurate determination above 75 km. For more details, see *Ortland et al.* [1998].

The space-time coverage of HRDI data depends on the 96 min UARS orbital period, the 57° orbital inclination and the 72 day orbital precession rate. The HRDI telescope views at a pair of 45° angles from the orbit normal. A tangent point track intersects a latitude circle twice within its coverage range, once in the ascending node and once in the descending node. At the latitude of TMF only one of these nodes occurs during the day time (when HRDI can make temperature measurements). The orbital period and precession rate determine that consecutive orbit crossings occur 24.4° in longitude apart. This means that the closest pair of crossings will occur after 15 orbits (one day), and the second of these will be 6° longitude to the west of the first. At the latitude of TMF, this gives a separation of 540 km, with a 20 min local time delay, and eventually a HRDI overpass of TMF within 500 km once every ~4 days. Sufficient information was not available from the geographical near-coincidences alone. Therefore, to obtain a significant statistical basis, all longitudinally averaged HRDI temperature profiles taken in January and February between 1994-1997 at the latitude of TMF were used. A total of 109 profiles distributed over 8 hours between 8:30 and 16:30 LST were used for a comparison with the TMF lidar winter results.

3. Nighttime evolution of temperature: Comparison of lidar, HRDI, and GSWM.

Figure 1 shows the evolution of the hourly-mean temperature profiles obtained by lidar at TMF for 3 consecutive nights in January 1997 and 5 consecutive nights in February 1998. The first profile was taken at the beginning of the night (19:00 LST for January 97 and 20:00 LST for February 98) and the others are shifted by 10 K every one hour, ending at 5:00 LST. The profile separated from the others on the right is the overall nightly average profile. The dotted-dashed line is the January monthly-mean temperature

profile from CIRA-86 [Fleming *et al.*, 1990]. A mesospheric temperature inversion layer (grey shaded areas) is consistently observed between 60 and 70 km altitude. The consistency is not only observed between two consecutive nights but also between January 1997 and February 1998. Moreover, the top of the temperature inversion appears to show a characteristic behavior; its altitude decreases from near 65-70 km at the beginning of the night to near 60-65 km at the end of the night. This strong night-to-night repeatability in the inversion behavior might mean that tidal effects act as a major source of variability in this region. However, at this stage of the analysis it is difficult to assert that they are entirely responsible for the formation of the inversions. Too much variability in time, a non-systematic downward propagation (some stationary and/or upward propagating structures have been also observed, not shown here), and especially some 10-30 K amplitude would argue against this.

The raw lidar data for each of the 5 nights of January 1997 were combined to obtain mean nighttime profiles for January 1997, sampled every hour between 18:00 and 5:00 LST. The same method was employed to obtain mean nighttime profiles for February 1998, and similarly profiles combining January 1997 and February 1998. These hourly-mean profiles for January 97, February 98, and both periods together, are presented in figure 2. As expected, and compared to figure 1, a large part of the temperature variability has been removed and the smoothed appearance of each profile shows that most of the geophysical and instrumental noise has been suppressed. The temperature inversion layers at 60-70 km are still present in all three figures (shaded areas) and their amplitudes remain moderate. Although they are not as strong as the inversions observed in the individual profiles, it is clear that these inversions are not the result of a random or chaotic behavior. The ratios of the amplitude of the individual inversions (15-30 K) to the amplitude of the mean inversions (10-15 K) are much larger than the number of profiles used to obtain the mean profiles (approximately 10 hourly individual profiles were used to obtain one hourly mean profile), indicating that the inversion layers have a repetitive behavior on a day-to-day basis. The nightly average profiles have been initialized at altitudes higher than 90-95 km, thus giving a high level of confidence below 80 km. A well defined wave-like structure can be observed above 80 km with a

temperature minimum propagating downward during the night. For some profiles, a second temperature inversion layer occurring between 80 and 90 km altitude is also observed. This structure is very similar to that observed 20 km lower and, as discussed below, might help confirm the role of the tides. Figures 1 and 2 additionally show that the temperature inversions cannot be a consequence of the semidiurnal component alone since all of the nightly mean profiles (close to 12-hour averages) show a well defined non-zero wave amplitude.

For the three periods defined above, the nightly average profile was subtracted from each of the hourly mean profiles. This calculation was also made for the daytime HRDI temperatures obtained at the latitude of TMF in January and February 1994-1997 (but using the daytime average instead of the nighttime average). The temperature differences obtained by lidar every hour between 18:00 and 5:00 LST and by HRDI between 8:30 and 16:30 LST are contoured as a function of altitude and time in plate 1. Due to the limited statistics, the HRDI data cannot be displayed for each year separately and therefore any interannual tidal variability could introduce some small differences between HRDI and lidar. These differences are expected to be negligible compared to the tidal amplitudes and to the residual noise contained in both HRDI and lidar datasets. It should also be noted that the HRDI daily average temperature and the lidar nightly average temperature can be very different. Moreover, unlike the ground-based lidar, the zonal averaging of the HRDI temperatures will tend to remove any local or regional effect. Consequently, a perfect consistency between the observed structures in the lidar and HRDI temperature differences should not be expected unless a strong tidal component is present (i.e., large amplitudes are involved). This is actually the case for a well defined warm period propagating downward from 100 km at 10:00 LST (HRDI dataset) to 75 km at 20:00 LST (lidar dataset) observed in both January 1997 and February 1998. Also well defined in the lidar data is a thin layer of strong temperature change between 60 and 70 km, the result of downward propagating temperature inversions, and a wide layer of continuous cooling between 40 and 60 km, especially visible in February 1998, all highly consistent with

previous observations at winter midlatitudes [Gille *et al.*, 1991]. Even though a LST dependence is evident it is still difficult to assign this unequivocally to a tidal origin.

The next step is to compare these observed temperature differences to the corresponding values calculated from the outputs of tidal models. The diurnal and semidiurnal phases and amplitudes from GSWM were used to compute the GSWM temperature differences from the daytime and nighttime averages. Assuming GSWM temperatures defined by:

$$T(z, t)_{|GSWM} = \overline{T_o}(z) + A_{24}(z) \cos\left(\frac{2\pi}{24}(t - \varphi_{24}(z))\right) + A_{12}(z) \cos\left(\frac{2\pi}{12}(t - \varphi_{12}(z))\right) \quad (1)$$

where $\overline{T_o}$ is the diurnal mean temperature (i.e. 24-hour average) and A_{24} , A_{12} , φ_{24} , φ_{12} are the amplitudes and phases of the diurnal and semidiurnal components given by GSWM, the daytime average (between 8:00 and 16:00 LST) can be calculated as follows:

$$\overline{T_d}(z)_{|GSWM} = \frac{1}{8} \sum_{t=8}^{16} \left(\overline{T_o}(z) + A_{24}(z) \cos\left(\frac{2\pi}{24}(t - \varphi_{24}(z))\right) + A_{12}(z) \cos\left(\frac{2\pi}{12}(t - \varphi_{12}(z))\right) \right) \quad (2)$$

and the temperature difference from the daytime average is:

$$\begin{aligned} T(t, z) - \overline{T_d}(z)_{|GSWM} &= A_{24}(z) \cos\left(\frac{2\pi}{24}(t - \varphi_{24}(z))\right) + A_{12}(z) \cos\left(\frac{2\pi}{12}(t - \varphi_{12}(z))\right) \\ &\quad - \frac{1}{8} \sum_{t=8}^{16} \left(A_{24}(z) \cos\left(\frac{2\pi}{24}(t - \varphi_{24}(z))\right) + A_{12}(z) \cos\left(\frac{2\pi}{12}(t - \varphi_{12}(z))\right) \right) \end{aligned} \quad (3)$$

Similarly, the difference from the nighttime average (between 19:00 and 5:00 LST) can be calculated:

$$\begin{aligned} T(t, z) - \overline{T_n}(z)_{|GSWM} &= A_{24}(z) \cos\left(\frac{2\pi}{24}(t - \varphi_{24}(z))\right) + A_{12}(z) \cos\left(\frac{2\pi}{12}(t - \varphi_{12}(z))\right) \\ &\quad - \frac{1}{10} \sum_{t=19}^5 \left(A_{24}(z) \cos\left(\frac{2\pi}{24}(t - \varphi_{24}(z))\right) + A_{12}(z) \cos\left(\frac{2\pi}{12}(t - \varphi_{12}(z))\right) \right) \end{aligned} \quad (4)$$

The temperature differences from the daytime and nighttime averages predicted by GSWM in January at the latitude of TMF are plotted in plate 2 with the same scales as plate 1. This way, the lidar and HRDI results can be directly compared to GSWM. Since it has frequently been found that observed diurnal and semidiurnal amplitudes and those predicted by GSWM differ by at least a factor of two [Dao *et al.*, 1995; Yu *et al.*, 1997; States and Gardner, 1998], the differences plotted in plate 2 were determined by doubling the GSWM values. In all following plots and discussion the GSWM amplitudes are twice the amplitudes actually predicted by GSWM.

Remarkable similarities are found between lidar, HRDI, and GSWM results. First the downward propagating warm period shown in plate 1 is also predicted by GSWM but two to three hours later than actually observed by HRDI. The warm early night and cold late night observed between 40 and 60 km is also predicted by GSWM but between 40 and 55 km. The cold early night and warm late night observed by lidar in the thin layer 65-70 km (result of the downward propagating temperature inversion) is also predicted, between 55 and 65 km, by GSWM but with a much smaller amplitude. This last result would indicate that the mesospheric temperature inversions observed above TMF in winter are the result of the combined effect of the diurnal and semidiurnal components. Finally, although some geophysical and instrumental noise remains above 75 km in the lidar data it seems that the beginning of the night is warmer than the end of the night, especially in January 97. This is still observed in February 98 but with a weaker amplitude. Again this is in good agreement with GSWM which predicts a larger effect of the semidiurnal component in January than in April (not shown). The main features predicted by GSWM are also observed by HRDI. Colder periods between 8:00 and 10:00 LST around 90-95 km, and between 13:00 and 15:00 LST around 70-80 km, and warmer periods at 8:00-9:00 LST below 75 km and propagating downward during the all day from 105 km to 85 km.

4. Determination of the diurnal and semidiurnal tidal components from a 10-hour nighttime measurement window.

Plates 1 and 2 clearly show the points of agreement and disagreement between lidar, HRDI, and GSWM. The next step is to try to extract the diurnal and semidiurnal components from the lidar observations. As indicated in the introduction, fitting both 12- and 24-hour components using an 8- to 11-hour wide measurement window can be tricky if not hazardous. For this reason, some simulations were made to insure that the methods described below were relevant and reliable. The tests consisted of calculating 24 simulated temperature profiles (1 every hour) using given amplitudes and phases of propagating diurnal and semidiurnal components. To optimize the tests, the diurnal vertical wavelength was assigned to be 20 km with a phase at 00:00 at 50 km. The semidiurnal vertical wavelength was assigned to be 30 km with a phase at 00:00 at 50 km and the amplitudes of both components were set to be constant with height throughout the entire middle atmosphere. Thus the repetition of the modulation of one component by the other is covered entirely in a 60-km range and one can focus on the real problem, i.e., the effect of undersampling. The tests were made with 3 simulation configurations. In the first configuration (I), the amplitudes of the diurnal and semidiurnal components were the same and equal to 2 K. In the second configuration (II), the semidiurnal amplitude was 4 K and the diurnal amplitude was 1 K. In the third configuration (III), the semidiurnal amplitude was 1 K and the diurnal amplitude was 4 K. This allowed the determination of the effect of a dominant component. Since we are focusing on the effect of the amplitudes and the effect of the undersampling, no noise nor geophysical disturbances other than tides were introduced.

Figure 3 shows the effect of fitting the simulated profiles with the configuration (I) over a 10-hour measurement window (here 18:00 - 4:00 LST) using the difference from the true 24-hour average. For brevity, only the results from configuration (I) will be shown in this paper. The actual amplitudes and phases are plotted with triangles and the amplitudes and phases calculated by the fits are plotted with

circles and error bars. Figure 4 is similar to figure 3 but using the differences from the 10-hour average instead of the true 24-hour average. As expected, when the 10-hour average is used the extraction of the diurnal and semidiurnal components is not necessarily correct. Two major conclusions emerge from the results from all three configurations. First, a component with a small amplitude compared to the other can never be retrieved correctly (configurations II and III, not shown). Second, when its amplitude is large enough, the semidiurnal component can be correctly retrieved (figure 4, right plots). Also, when its amplitude is large enough the diurnal component can be determined but not directly from the results of the fit. It can be seen from figure 4 that fitting over a 10-hour wide window will give a repetitive pattern in the diurnal calculated phase with an alternation of regions of nearly-constant phase with height and regions of undetermined phase. This periodic pattern is dictated by the location and width of the measurement window. The regions of constant phase with height are always located in quarter-phase with the center of the measurement window. The reason is that, in this region, the cosine function crosses zero near the center of the window and the resulting 10-hour average will be close or equal to the true 24-hour average. Where the associated standard deviation of the phase is minimum and the associated amplitude is maximum, the fit will converge to the correct values of both amplitude and phase of the diurnal component even if fitted over a 10-hour window, as illustrated by figure 3. Using the same argument, it appears that the regions of undetermined phase are always located in phase or out-of-phase with the center of the measurement window, and the associated amplitude will be calculated as near-zero. In the case of figure 4 the measurement window is 18:00 - 04:00 LST (close to a standard night), centered on 23:00 LST. Then the regions of constant phase with height are in quarter-phase with 23:00 LST, i.e., 17:00 and 5:00 LST, and the regions of undetermined phase are in phase and out-of-phase with 23:00 LST, i.e., 11:00 and 23:00 LST. To ensure that this pattern is obtained wherever the measurement window is located, this latter was shifted 8 times by 3-hours and each time a similar pattern was obtained. This method of diurnal phase determination is very useful when the diurnal phase is expected to propagate downward over at least one vertical wavelength and when the diurnal amplitude is not too small compared to the semidiurnal. It is not applicable when the diurnal amplitude is too small compared

to the semidiurnal (configuration II, not shown). Although this method is not always applicable in the stratosphere and mesosphere we will see below how useful it appears to be in the case of TMF.

5. Diurnal and semidiurnal tidal components calculated from lidar measurements.

Figure 5 shows the results of the 2-component fits applied to the GSWM differences from the 10-hour average plotted in plate 2 between 19:00 and 5:00 LST. The true GSWM diurnal and semidiurnal amplitudes ($\times 2$) are plotted with solid lines and the amplitudes calculated by the fits are plotted with solid lines with error bars. The true GSWM diurnal and semidiurnal phases are plotted with triangles and the results from the fits are plotted with circles and error bars. As explained above, the regions of constant diurnal phase with height are located near 18:00 and 6:00 LST and the regions of undetermined phase are located at 12:00 and 00:00 LST. It is clear that a basic phase interpolation between the regions of maximum calculated diurnal amplitude associated with constant diurnal phase with height and minimum standard deviation on diurnal phase and the regions of undetermined diurnal phase associated with near-zero diurnal amplitude will give a correct estimation of the diurnal phase. Also, when the semidiurnal amplitude is not too small compared to the diurnal amplitude (i.e. above 55-60 km), the semidiurnal phase is correctly calculated. Figure 6 is similar to figure 5 but the fit is now applied to the lidar data plotted in Plate 1(b) (February 1998). The GSWM diurnal and semidiurnal amplitudes are plotted with solid lines and the amplitudes calculated by the fits are plotted with solid lines with error bars. The GSWM diurnal and semidiurnal phases are plotted with triangles and the results from the fits are plotted with circles and error bars. On the diurnal phase plot, the altitude of each characteristic region is now shifted by a few kilometers compared to GSWM. This altitude shift was already observed when comparing plates 1 and 2. This confirms that the diurnal phases predicted by GSWM and observed by lidar are consistent so long as we take into account this observed altitude shift. The layer of fast phase transition (calculated at 53-58 km by GSWM and observed at 57-60 km by lidar) points out the transition between the dominance of the forced modes trapped into the upper stratosphere and the propagating modes into the mesosphere. An estimation of the correct diurnal phases and amplitudes can be made by comparison with the diurnal

phases and amplitudes given by GSWM as a "first guess". The diurnal phase seems to have been well tracked, propagating downward from 8:00 LST at 83 km to 18:00 LST at 73 km with a maximum associated amplitude, 6:00 LST at 60 km and again 18:00 LST at 57 km. Then, it remains constant (~18:00 LST) down to 40 km, as predicted by GSWM. However, the semidiurnal amplitude calculated by the fit remains small below 70 km, with some occasional peaks occurring at 40 and 60 km. Except at these altitudes, the calculated semidiurnal phases are inaccurate and no result on the semidiurnal tide can be obtained directly from the fit. In particular, the apparent downward propagation between 65 and 60 km of the semidiurnal phase from 4:00 LST to 8:00 LST is a misinterpretation by the fit and is actually the result of the downward propagation of the diurnal phase. By comparing plates 1 and 2, and by taking the values of the semidiurnal phase where the associated standard deviation is minimum and the associated amplitude is maximum, it is possible to have sporadic estimations of the semidiurnal component. Actually, they appear to be very close to the semidiurnal phases and amplitudes given by GSWM. Once the estimated diurnal and semidiurnal components have been determined, the last step is to ensure that they correspond to the observations. Plate 3 is similar to plate 2 but using the newly estimated components instead of GSWM. Our new estimations are available only between 40 and 84 km. Below 40 km the amplitudes are too small and above 84 km the lidar data are affected by noise and initialization so that no estimation was attempted. The agreement with both lidar and HRDI (plate 1) is remarkable. The warm early night and cold late night between 40 and 60 km have similar amplitudes, the warming trend in the thin layer 65-70 km is well reproduced, with now much larger amplitude than calculated by GSWM. Also the warm early night and cold late night above 70 km is well reproduced. The agreement with HRDI is good too; warm early day at 70 km, a cold period at 13:00 LST and 85 km and at 14:00-15:00 LST at 65 km, then a warmer late day at 84 km and below.

To verify that our estimations are correct, a 24-hour average profile was estimated and used to re-apply a two-component fit to the lidar data. Using each of the ten hourly composite profiles (from 19:00 to 5:00

LST) and our estimations of the diurnal and semidiurnal phase and amplitude, ten 24-hour averaged profiles were calculated:

$$\overline{T_0^{t_i}}^E(z) = T(z, t_i) - A_{24}^E(z) \cos\left(\frac{2\pi}{24}(t_i - \phi_{24}^E(z))\right) - A_{12}^E(z) \cos\left(\frac{2\pi}{12}(t_i - \phi_{12}^E(z))\right) \quad (8)$$

Then a singular 24-hour average profile was obtained by taking the average:

$$\overline{T_0}^E(z) = \frac{1}{10} \sum_{t_i=19}^5 \overline{T_0^{t_i}}^E(z) \quad (9)$$

If the estimated phases and amplitudes are correct, the newly estimated 24-hour average $\overline{T_0}^E(z)$ will be equal or close to each of the 24-hour averaged profiles $\overline{T_0^{t_i}}^E(z)$ (small rms.) and the results from the fit applied to the differences from this 24-hour average will converge to the true components (as illustrated by figure 3) and will no longer indicate regions of constant diurnal phase with height and regions of undetermined diurnal phase. Figure 7 is similar to figure 6 but using the estimated 24-hour average instead of the 10-hour average. The estimated diurnal and semidiurnal amplitudes are plotted with solid lines and the amplitudes calculated by the fits are plotted with solid lines with error bars. The estimated diurnal and semidiurnal phases are plotted with triangles and the results from the fits are plotted with circles and error bars. As expected, there are no longer alternate regions of constant diurnal phase with height and regions of undetermined diurnal phase. Actually the regions of constant phase with height displayed here between 40 and 55 km are representative of a real atmosphere (forced modes) and the region of apparently undetermined diurnal phase at 58 km is due to the transition from the dominant forced modes with a diurnal phase at 17:00 LST below 55 km to the propagating modes with a diurnal phase at 5:00 LST at 59 km. The amplitude associated to the latter modes reaches 7 to 10 K at 65 km. Also expected is still the large uncertainty in the determination of the semidiurnal component due to its weak amplitude compared to the diurnal component. Except for two points at 42 km (and 60 km) with a

semidiurnal amplitude of 2 K (and 3 K respectively) and a semidiurnal phase of 11:00 LST (and 9:00 LST respectively), the fits have not converged to the estimated semidiurnal phases and amplitudes.

6. Discussion and conclusion.

A total of 140 hours of nighttime lidar measurements (30-85 km) taken in January 1997 and February 1998 at Table Mountain Facility (34.4°N) have been used to study the possible signature of the middle atmospheric thermal tides. Some of the results have been shown together with the zonally averaged daytime HRDI temperature profiles (65-105 km) taken at the same season and latitude between 1994 and 1997.

Persistent temperature inversions have been observed by lidar at 60-70 km altitude in both January 1997 and February 1998, with a repetitive behavior from day-to-day, suggesting a significant role is played by the tides. For the two separate periods defined above and for the two periods taken together, the nightly-average profile was subtracted from each of the hourly-mean profiles. This calculation was also made for HRDI using the daytime average instead of the nighttime average. The temperature differences obtained by lidar every hour between 18:00 and 5:00 LST and by HRDI between 8:30 and 16:30 LST were compared to their equivalent calculated by the tidal model GSWM. Although local effects (like sun-synchronous long-period gravity wave) are removed by the zonal averaging, a remarkably consistent structure between HRDI and lidar has been identified, namely the downward propagation of warm temperatures from 100 km at 10:00 LST to 75 km at 20:00 LST and 65-70 km at 3:00-5:00 LST surrounded above and below by its colder counterparts (plate 1). At the lower end of this structure (60-70 km) the warm late night following the cold early night has been found to be associated with the downward propagation of the temperature inversion layers (figure 2). Relatively good agreement was observed between both HRDI and lidar observations and GSWM, especially between lidar and GSWM below 58 km. The points of disagreement are mainly quantitative:

- 1) First, and it is not new, the amplitudes calculated by GSWM are much smaller than those observed (at least a factor of 2).
- 2) There is a 3-hour delay in the downward propagation of the warm temperatures between 105 and 80 km altitude as calculated by GSWM compared to HRDI.
- 3) The warm late night following the cold early night in the lower mesosphere is observed around 63 km altitude by lidar while it is calculated around 58 km by GSWM.

The disagreement in 1) and 2) is substantially reduced for altitudes above 80 km if the recently revised GSWM98 model is used [*Hagan*, Private communication]. In this new model, the background winds and Rayleigh friction have been modified. The model now incorporates a 6-year database of HRDI, HALOE (below 50 km), and MLS (above 50 km) monthly, averaged data. The main consequences of these changes are increases in the diurnal and semidiurnal amplitudes, and a counterclockwise phase shift of about 1 to 4 hours (or an equivalent downward altitude shift of 4-7 km in phase) compared to the older GSWM, depending on the altitude. However, the amplitude ratio between observations and GSWM98 is still large for altitudes below 80 km. Furthermore, the altitude shift observed for the layer of fast phase transition (58-63 km) is not reduced and is even slightly increased. From the observations it is clear that the structured layer between 60 and 70 km altitude is LST related. Now the logically occurring question is: Is this layer the result of a purely tidal signature, or is there a local effect (such as a 24-h period gravity wave forced in the lower atmosphere), or could it be the result of coupling between gravity waves and tides? The suggestion of a local effect seems to be less probable since the temperature inversions and their LST-related behavior have been frequently observed at different locations [*Leblanc and Hauchecorne*, 1997; *States et al.*, 1998; *Meriwether et al.*, 1998] preferentially suggesting a more global effect. Therefore in the following discussion, we will focus only on the two possible effects of pure tidal oscillations and gravity wave-tidal coupling.

Assuming that the lidar observations in the mesosphere and, in particular, the temperature inversions are representative of a pure tidal signature, a major theoretical barrier has to be overcome. How large can the diurnal and semidiurnal amplitudes be at 70 km altitude to lead to inversions with frequent 25 K amplitudes? Using a "first guess" method and using simulated data, the diurnal and semidiurnal phases and amplitudes have been estimated using the nighttime lidar profiles (sections 4 and 5). While the semidiurnal component remains smaller than the diurnal component (especially below 70 km) and consequently could not be correctly estimated in the entire middle atmosphere, the diurnal component has been clearly identified. It appears that the estimated diurnal amplitude and phase are qualitatively close to those calculated by GSWM but shifted by a few kilometers in altitude (figures 5 and 6). In particular, the fast phase transition calculated to be around 58 km by GSWM and corresponding to the transition between the upper stratospheric forced (trapped) modes and the upward propagating modes has been estimated using the lidar data to be around 63 km, i.e., ~5 km higher. Immediately above this altitude the warm late night following the cold early night is the consequence of a fast growing diurnal amplitude with height. However, this behavior is contained in only a 5-8 km thin layer because of the emergence of the semidiurnal component at upper altitudes. This latter together with the diurnal component is responsible for the warm early night then cold late night observed between 70 km and 75 km. The estimated diurnal amplitude has a minimum at 58 km (transition between trapped and propagating modes) and a maximum of 6.5 K at 65 km, with an associated phase around 2:00 LST. The diurnal amplitude calculated by GSWM has its minimum at 56 km and a maximum of 2.5 K around 72 km. The estimated semidiurnal phase is close to that of GSWM, with still a factor of two between the calculated and estimated amplitudes. Thus, using estimated components qualitatively close to those calculated by GSWM it is possible to reproduce adequately the nighttime behavior of the temperature inversions. The cold bottom part of the inversion is mainly governed by the diurnal oscillation while the warm top part of the inversion is actually governed by both the diurnal and semidiurnal oscillations. Above 75 km, the semidiurnal component is dominant and leads to a cold midnight and warm late night above 82 km (plate 3). The resulting temperature profile above 75 km therefore shows the downward propagation of a second

inversion with its bottom observable on the lidar data at the beginning of the night near 85 km and at the end of the night around 80 km altitude (figure 2). However, the estimation of the tidal components in the layer 82-86 km remains approximate due to the increasing noise in the lidar data above 80 km. Using both daytime and nighttime Sodium lidar measurements above Urbana, IL (40°N) in fall, *States and Gardner* [1998] have observed between 84 and 94 km a diurnal phase close to that of GSWM, which would confirm, despite the difference in season and latitude, our current estimations. Unfortunately, they did not provide any information on the semidiurnal component, but their figure 1 points out at 83 km a cold period at 18:00-20:00 LST then warmer temperatures (relative to the nightly-mean) at 6:00-8:00 LST, accompanied by two temperature minima within the 24-h window between 83 and 86 km, which is consistent with the temperature behavior observed in our figure 2 and to our estimations of the diurnal and semidiurnal phases. Although our estimated components have been calculated using the nighttime data only, they appear to agree remarkably well with the results from the daytime HRDI measurements (plates 1 and 3). A warm early day between 65 and 80 km, then a generally cold period between 12:00 and 15:00 LST below 85 km, then a warmer period propagating downward and just observable below 85 km after 15:00 LST (very end of the HRDI daytime window).

Although it has been shown that it is at least qualitatively possible to explain the formation of the temperature inversions with the effect of pure tidal oscillations, the alternative explanation of a gravity wave-tidal coupling is not unlikely. Indeed, using 2D numerical modeling [*Liu and Hagan*, 1998] have shown that the altitude and severity of the gravity wave breaking and its consequences can be strongly influenced by the background wind, especially the tidal wind. The gravity wave breaks preferentially in the region of strong vertical shear with the same sign as that of the gravity wave phase speed. Then, turbulence, diffusion and advection lead to cooling and heating layers, following the same mechanisms as in previous modeling of gravity wave-mean flow interaction [see for example, *Holton*, 1983; *Hauchecorne and Maillard*, 1990; *Fritts et al.*, 1996]. The difference to previous modeling is the LST dependence of the vertical shear (or in case of wave overturning the suradiabatic temperature gradient)

and consequently the LST dependence of the formation of the inversions. This LST- and, especially, gravity wave-related mechanism would clarify two major striking features which have not been elucidated previously. The strong day-to-day variability observed in many cases and the large amplitudes, sometimes reaching 35-40 K at winter midlatitudes [*Leblanc and Hauchecorne, 1997*]. In addition, the simulations are able to produce a second temperature inversion (multiple breaking levels) located one vertical wavelength higher which is consistent with the observations (see figure 2 and *States and Gardner [1998]*).

At this time, there are no available observations capable of favoring either of the two possible mechanisms described above. The similarities between the observations and the outputs from GSWM are remarkable but there is still a large disagreement in the amplitudes involved to assert that purely tidal oscillations are responsible for the formation of the temperature inversions. On the other hand, numerical modeling has shown that LST-dependent temperature inversions can develop after gravity breaking but the mechanistic model used in that case is at an early stage of development and more simulations have to be made to locate and quantify more precisely the resulting mesospheric heating and cooling. More winter nighttime lidar observations are planned at TMF and it is hoped that future results will allow our estimations of the tidal components to be refined and perhaps have a better understanding of the middle atmospheric thermal structure at midlatitude in winter.

Acknowledgements

The work described in this paper was carried out at the Jet Propulsion Laboratory, California Institute of Technology under an agreement with the National Aeronautics and Space Administration. We are extremely grateful to Maura Hagan and Hanli Liu (NCAR) for invaluable discussions regarding GSWM and mesospheric tides.

References.

- Burrage, M. D., R. A. Vincent, H. G. Mayr, W. R. Skinner, N. F. Arnold and P. B. Hays, Long-term variability in the solar diurnal tide observed by HRDI and simulated by the GSWM, *Geophys. Res. Lett.*, 22, 2641-2644, 1995.
- Chapman S., and R. S. Lindzen, *Atmospheric tides*, 201 pp., D. Reidel, Norwell, Mass., 1970.
- Dao, P. D., R. Farley, X. Tao, and C. S. Gardner, Lidar observations of the temperature profile between 25 and 103 km: evidence of strong tidal perturbation, *Geophys. Res. Lett.*, 22, 2825-2828, 1995.
- Dudhia, A., S. E. Smith, A. R. Wood, and F. W. Taylor, Diurnal and semidiurnal temperature variability of the middle atmosphere, as observed by ISAMS, *Geophys. Res. Lett.*, 20, 1251-1254, 1993.
- Fleming, E. L., S. Chandra, J. J. Barnett and M. Corney, COSPAR International Reference Atmosphere, Chapter 2: Zonal mean temperature, pressure, zonal wind and geopotential height as functions of latitude, *Adv. Space Res.*, 10 (12), 11-59, 1990.
- Forbes, J. M., Atmospheric tides 1. Model description and results for the solar diurnal component, *J. Geophys. Res.*, 87, 5222-5240, 1982.
- Forbes, J. M., Tidal and planetary waves, *The upper mesosphere and lower thermosphere: A review of experiment and theory*, Geophysical Monograph 87, 67-87, 1995.
- Fritts, D. C., J. F. Gartin and Ø. Andreassen, Wave breaking and transition to turbulence in stratified shear flows. *J. Atmos. Sci.* 53, 1057-1085, 1996.
- Gille, S. T., A. Hauchecorne, and M. L. Chanin, Semidiurnal and diurnal tidal effects in the middle atmosphere as seen by Rayleigh lidar, *J. Geophys. Res.*, 96, 7579-7587, 1991.
- Hagan, M. E., J. M. Forbes and F. Vial, On modeling migrating solar tides, *Geophys. Res. Lett.*, 22, 893-896, 1995.

- Hauchecorne, A., and A. Maillard, A 2-D dynamical model of mesospheric temperature inversions in winter, *Geophys. Res. Lett.*, *17*, 2197-2200, 1990.
- Hedin, A. E., Extension of the MSIS thermosphere model into the middle and lower atmosphere, *J. Geophys. Res.*, *96*, 1159-1172, 1991.
- Holton, J. R., The influence of gravity wave breaking on the general circulation of the middle atmosphere, *J. Atmos. Sci.*, *40*, 2497-2507, 1983.
- Keckhut, P., A. Hauchecorne, and M. L. Chanin, A critical review of the database acquired for the long-term surveillance of the middle atmosphere by French Rayleigh lidars, *J. Atm. Ocean. Technol.*, *10*, 850-867, 1993.
- Keckhut, P., Gelmann M. E., Wild J. D., Tissot F., Miller A. J., Hauchecorne A., Chanin M.-L., Fishbein E. F., Gille J., Russell III J. M., and Taylor F. W., Semi-diurnal and diurnal tides (30-55 km): Climatology and effect on UARS-LIDAR data comparisons, *J. Geophys. Res.*, *101*, 10299-10310, 1996.
- Khattatov, B. V., V. A. Yubin, M. Geller, P. B. Hays and R. A. Vincent, Diurnal migrating tide as seen by the high-resolution Doppler imager/UARS 1. Monthly mean global meridional winds, *J. Geophys. Res.*, *102*, 4405-4422, 1997.
- Leblanc, T., and A. Hauchecorne, Recent observations of the mesospheric temperature inversions, *J. Geophys. Res.*, *102*, 19,471-19,482, 1997.
- Leblanc, T., I. S. McDermid, A. Hauchecorne, and P. Keckhut, Evaluation and optimization of lidar temperature analysis algorithms using simulated data, *J. Geophys. Res.*, *103*, 6177-6187, 1998a.
- Leblanc, T., I. S. McDermid, C. Y. She, D. A. Krueger, A. Hauchecorne, and P. Keckhut, temperature climatology of the middle atmosphere from long-term lidar measurements at mid- and low-latitudes, *J. Geophys. Res.*, (accepted), 1998b.

- Liu, H. -L., and M. E. Hagan, Local heating/cooling of the mesosphere due to gravity wave and tide coupling, *J. Geophys. Res.*, (submitted), 1998.
- Manson, A. H., C. E. Meek, H. Teitelbaum, F. Vial, R. Schminder, D. Kuschner, M. J. Smith, G. J. Fraser, and R. R. Clark, Climatologies of semi-diurnal and diurnal tides in the middle atmosphere (70-110 km) at middle latitudes (40-55°), *J. Atmos. Terr. Phys.*, *51*, 579-593, 1989.
- McDermid, I. S., S. Godin, and L. O. Lindqvist, Ground-based laser DIAL system for long-term measurements of stratospheric ozone, *Appl. Opt.*, *29*, 3603-3612, 1990.
- McLandress, C., G. G. Shepherd and B. H. Solheim, Satellite observations of thermospheric tides: Results from the Wind Imaging Interferometer on UARS, *J. Geophys. Res.*, *101*, 4093-4114, 1996.
- Meriwether, J. W., X. Gao, V. B. Wickwar, T. Wilkerson, K. Beissner, S. Collins, and M. E. Hagan, Observed coupling of the mesosphere inversion layer to the thermal tidal structure, *Geophys. Res. Lett.*, *25*, 1479-1482, 1998.
- Ortland, D.A. P.B. Hays, W.R. Skinner and J.-H. Yee, Remote sensing of mesospheric temperature and O₂(¹Σ) band volume emission rates with the high-resolution Doppler imager, *J. Geophys. Res.*, *103*, 1821-1835, 1998.
- States, R. J., and C. S. Gardner, Influence of the diurnal tide and thermospheric heat sources on the formation of mesospheric temperature inversion layers, *Geophys. Res. Lett.*, *25*, 1483-1486, 1998.
- Yu, J., R. States, S. J. Franke, C. S. Gardner and M. Hagan, Observations of tidal temperature and wind perturbations in the mesopause region above Urbana, IL (40°N, 88°W), *Geophys. Res. Lett.*, *24*, 1207-1210, 1997.

Figure Captions.

Figure 1. Nighttime evolution of hourly-mean temperature profiles measured by lidar at Table Mountain Facility, CA (TMF) between January 09 (a), and January 11 (c), 1997 and between February 27 (d) and March 03 (h), 1998. Each profile has been shifted by 10 K per hour starting at 19:00 LST or 20:00 LST and ending at 5:00 LST. The CIRA-86 monthly mean profile for January at 34.4°N is also displayed (dotted-dashed lines). The grey shaded areas correspond to observed temperature inversion layers.

Figure 2. Same as figure 1, but a) for the mean profiles of January 7-11, 1997, b) for the mean profiles of February 26-March 04, 1998, and c) for the mean profiles of January 1997 and February 1998 together.

Figure 3. Diurnal and semidiurnal phases (circles with error bars) and amplitudes (solid lines with error bars) calculated by fitting 10 simulated hourly-mean nighttime (from 18:00 to 4:00 LST) temperature profiles (departures from the true 24-hour average). The simulated diurnal and semidiurnal phases are plotted with triangles and the simulated amplitudes (2 K) are plotted with solid lines with no error bars.

Figure 4. Same as figure 3 but the fits were applied to the differences from the actual 10-hour average.

Figure 5. Diurnal and semidiurnal phases (circles with error bars) and amplitudes (solid lines with error bars) calculated by fitting 10 hourly-mean nighttime (from 19:00 to 5:00 LST) temperature profiles (departures from the 10-hour average) as calculated by GSWM at 34.4°N in January. The true GSWM components are plotted with triangles (phases) and solid lines with no error bars (amplitudes $\times 2$).

Figure 6. Same as figure 5, but for the TMF lidar temperature differences of February 1998 (see plate 1(b)) instead of GSWM. The true GSWM 34.4°N-January phases are plotted with triangles and the amplitudes ($\times 2$) with solid lines.

Figure 7. Same as figure 6, but using the differences from our own estimated 24-hour average instead of the actual 10-hour nighttime average. The estimated amplitudes are plotted with solid lines and no error bars and the estimated phases with triangles.

Plate Captions

Plate 1. Hourly-mean lidar (HRDI) temperature differences from their nighttime (daytime) average. a) lidar measurements at TMF during January 7-11, 1997, b) February 26-March 04, 1998, and c) January 1997 and February 1998 together. The mean lidar profiles of figure 2(a) to (c) have been used. For HRDI, all temperature profiles taken at the latitude of TMF in January and February 1994-1997 have been used.

Plate 2. Same as plate 1 but the temperature differences were calculated using the phases and twice the amplitudes of the diurnal and semidiurnal components predicted by GSWM at 34.4°N in January.

Plate 3. Same as plate 2 but using our own estimated diurnal and semidiurnal phases and amplitudes.

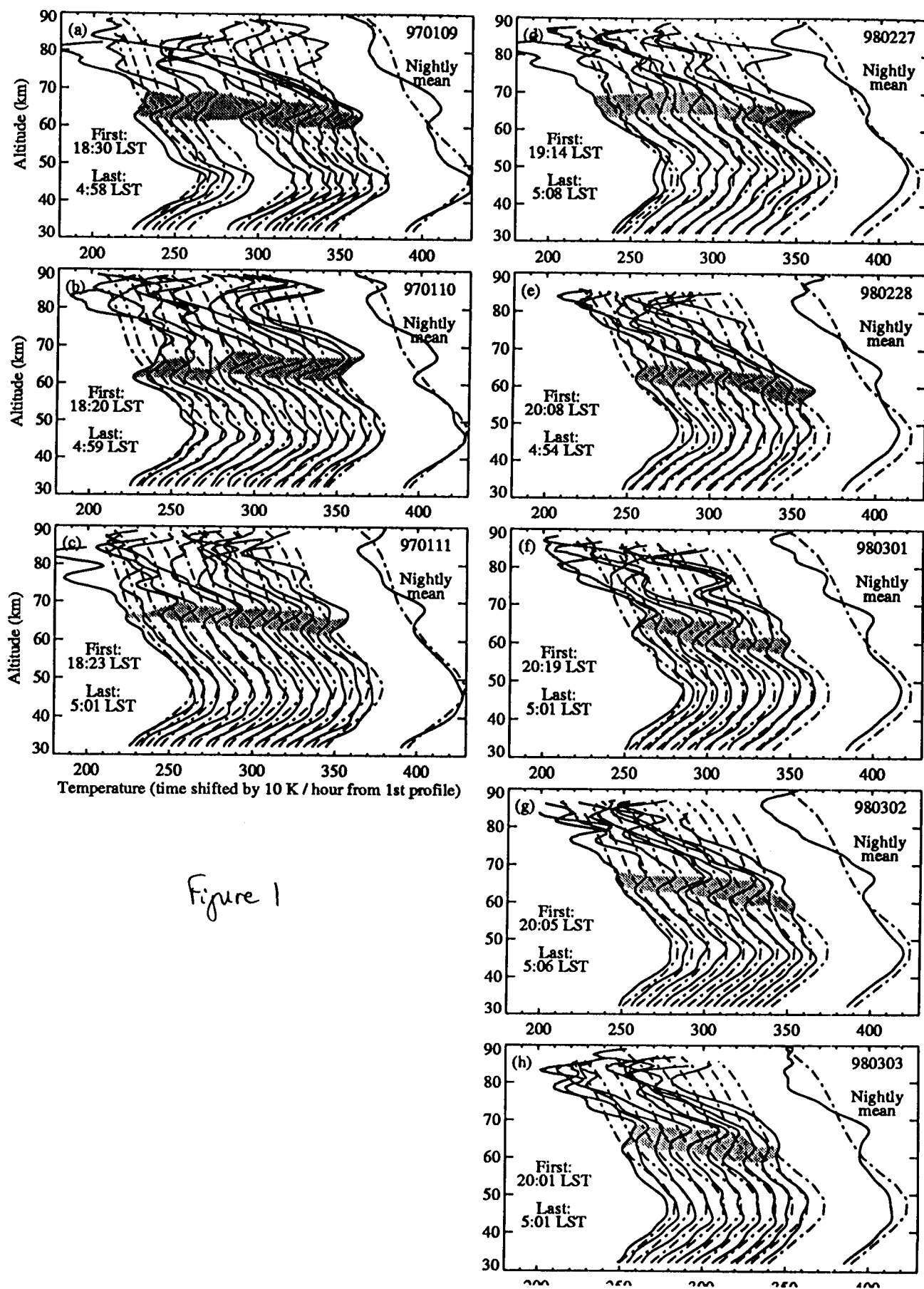


Figure 1

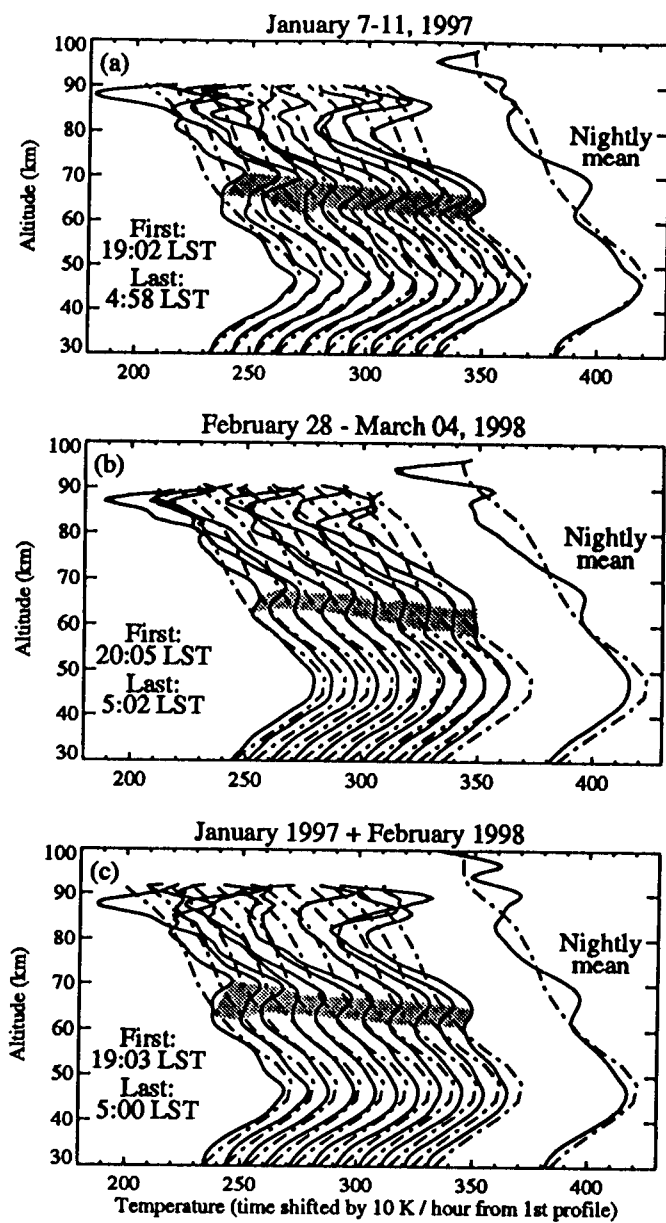


Figure 2

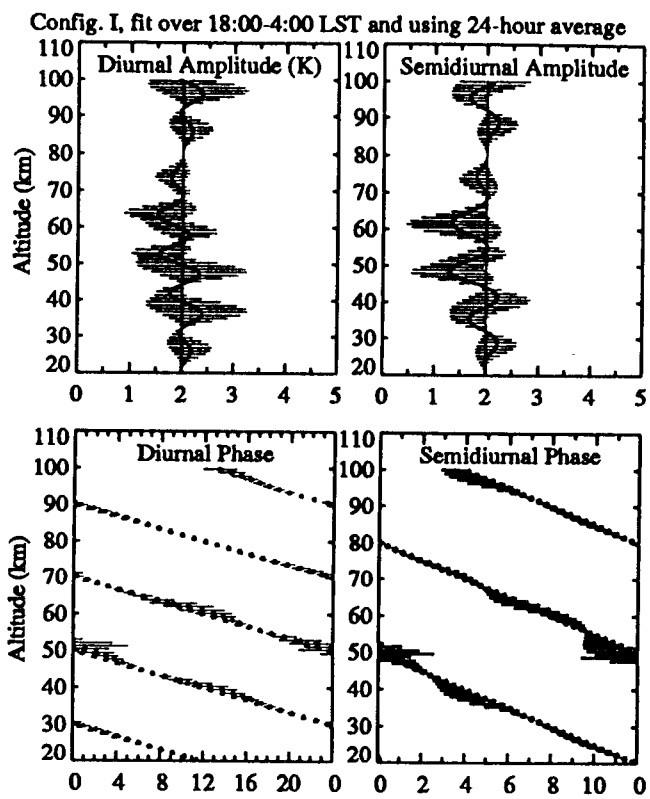


Figure 3

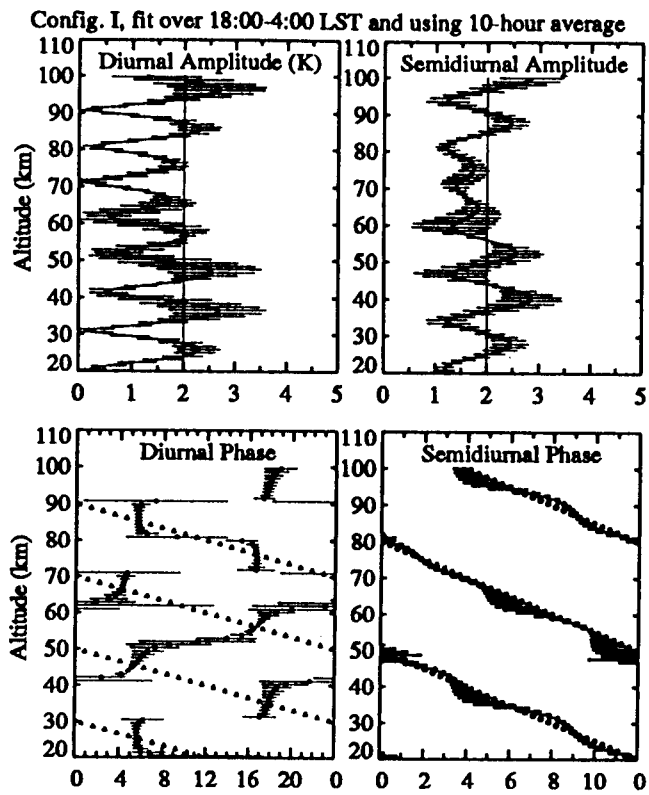


Figure 4

GSWM-Jan-34.4N, fit over 18:00-4:00 LST using 10-hour aver.

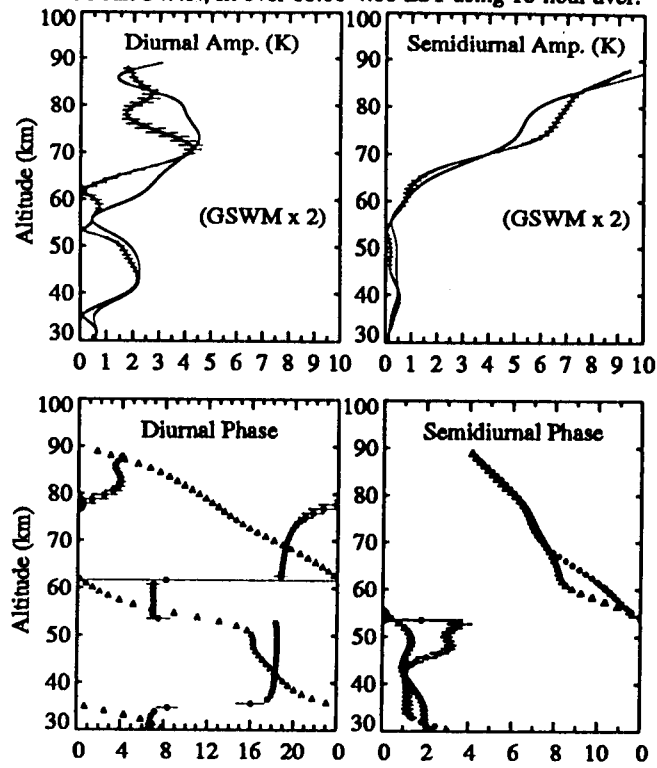


figure 5

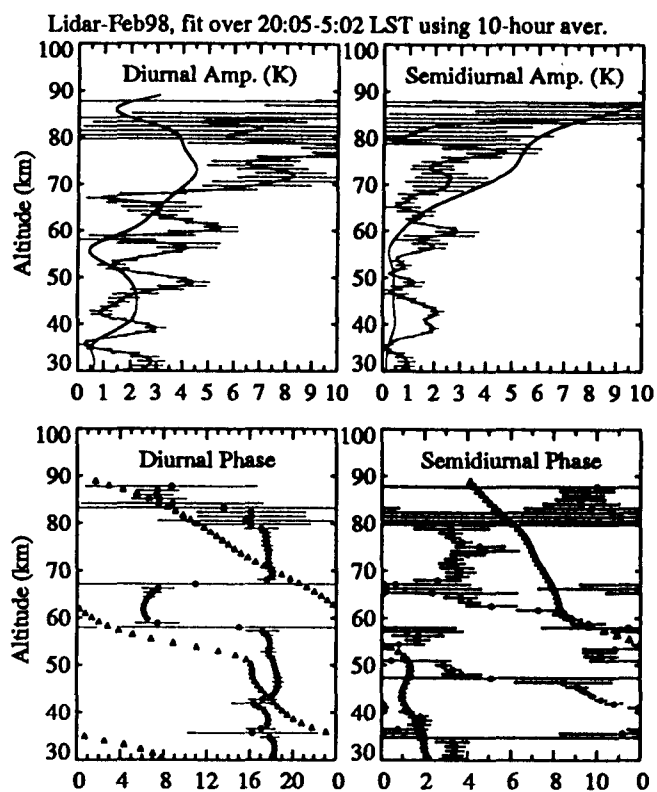


Figure 6

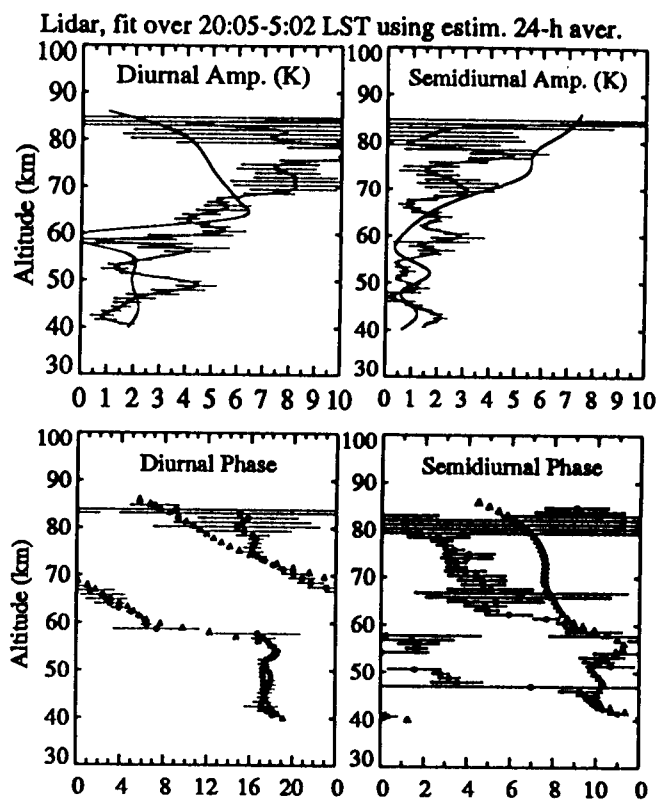


figure 7

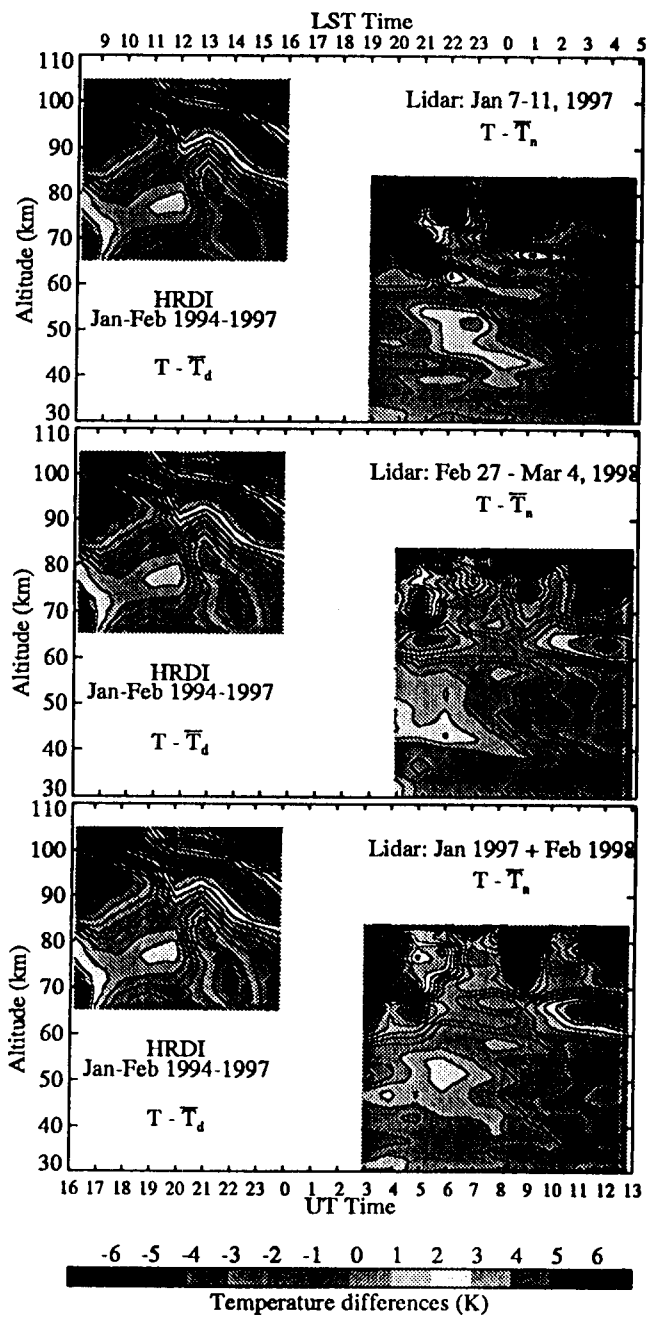


Plate 1

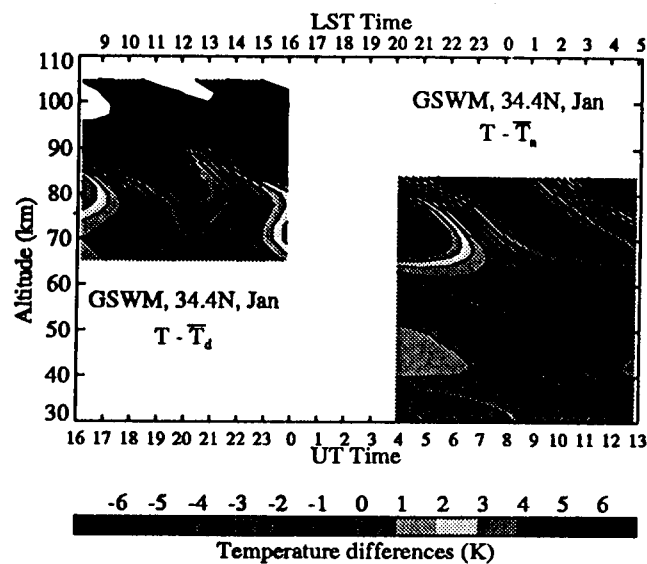


Plate 2

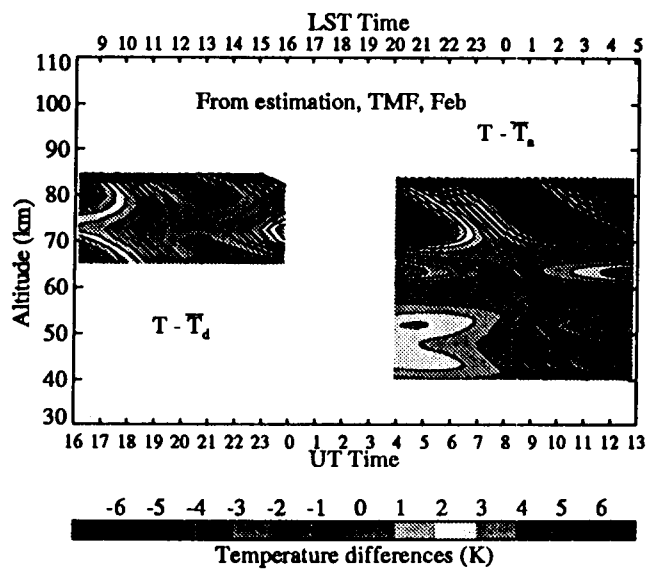


Plate 3